THE JOURNAL OF PHYSICAL CHEMISTRY C

Article

pubs.acs.org/JPCC

Voltage-Induced Transients in Methylammonium Lead Triiodide Probed by Dynamic Photoluminescence Spectroscopy

Daniel L. Jacobs,[†] Michael A. Scarpulla,[†,‡] Chen Wang,[†] Benjamin R. Bunes,[†] and Ling Zang*[,†]

[†]Materials Science and Engineering and [‡]Electrical & Computer Engineering, University of Utah, Salt Lake City, Utah 84112, United States

Supporting Information

ABSTRACT: In this work, we use time-resolved photoluminescence (PL) spectroscopy, microscopy, and current measurements to characterize the slow transient responses of methylammonium lead triiodide ($MAPbI_3$) on a lateral interdigitated electrode device. By systematically varying the applied bias magnitude and electrode polarity, we observed distinct reversible and irreversible PL transient responses in the form of spectrally and spatially resolved PL quenching occurring over a range of 0.5−100 s. When the simultaneous current and the PL measurements were correlated, the reversible responses, present under all electric fields, were attributed to charge trapping, whereas the irreversible response, occurring above a nominal electric field between 1 and 5 kV cm^{-1}, was attributed to ion migration. Thus, these results indicate that the slow transient response, and therefore hysteretic behavior, in $MAPbI_3$ devices is a complex response with contributions from both charge trapping and ion migration.

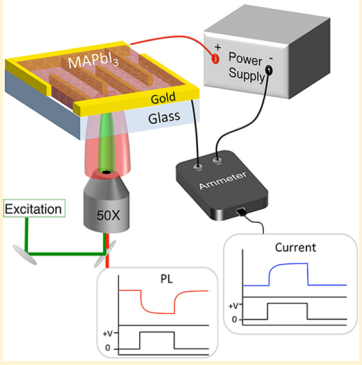

1. INTRODUCTION

Hybrid organic metal halide perovskites such as methylammonium lead triiodide ($MAPbI_3$) have shown remarkable promise for use in inexpensive and efficient solar cells.[1,2] Despite widespread research efforts and impressive performance improvements in less than a decade, many important and unusual physical properties and behaviors of these complex compounds must still be elucidated.[3] One critical behavior of these materials that is still not completely understood is the observation of electric field-induced transient behaviors occurring on the time scale of 1−100 s, collectively referred to as "slow transient effects". These effects have been documented in the form of hysteresis of illuminated current−voltage scans,[4−6] transients in photoconductivity,[5,7,8] effects in frequency-dependent measurements,[5,9−11] illumination-dependent dielectric constant,[12] and a switchable photovoltaic effect.[13−15] The slow transient responses lead to rate-dependent results, making it difficult to reliably report device efficiencies and repeat findings, and may also be related to performance decay over time even in inert environments.[16] Until the underlying mechanisms of these behaviors are fully understood, further device optimization will be a challenge. Theoretical and experimental results point to two leading hypotheses for the mechanism of these slow transient effects: (1) ion migration of charged shallow defects leading to native defect doping or buildup of space charge[8,13,17−20] or (2) charge trapping in interfacial electronic defects.[4,11] Previous studies have suggested that ferroelectric effects from methylammonium (MA^+) dipole alignment or lattice distortion may be an additional factor,[5,7,10,21−24] but recent work has discounted long-range ferroelectric effects at room temperature as a source of the slow transient response.[25−27] A majority of the experimental evidence supporting these leading theories come from electrical characterization methods on optimized photovoltaic (PV) devices or in specific test structures designed to investigate a finding or hypothesis from an optimized PV device, but most experiments are not able to differentiate between the different mechanisms or account for multiple mechanisms occurring simultaneously. Furthermore, the strong sensitivities of $MAPbI_3$ thin film properties to a number of factors, including morphology,[28−31] fabrication conditions,[32−35] and testing environment,[36−39] make it nearly impossible to compare results from different experiments. Therefore, it remains an open question whether the slow transient response arises from a single dominant mechanism in all samples or whether different subsets of several mechanisms are active in any given type of sample or device structure. Clearly, development of new and more universal testing platforms is necessary to deepen our understanding of this material system.

Photoluminescence (PL) is a powerful tool that has been essential to our current understanding of hybrid perovskite materials, elucidating properties such as chemical composition,[10,40,41] nanomorphology,[28] lattice structure,[42] interfacial charge transfer,[11,43−45] environmental sensitivity,[36,38,39] and charge carrier dynamics.[46−49] In most of these prior studies, the PL response was measured without electrical bias from films on glass, from partial device stacks without top contacts, or from complete device stacks through the transparent electrode in the open circuit state, meaning the measurements were all under steady-state conditions. A few noted exceptions have measured

Received: December 7, 2015
Revised: March 25, 2016
Published: March 25, 2016

DOI: 10.1021/acs.jpcc.5b11973
J. Phys. Chem. C 2016, 120, 7893−7902

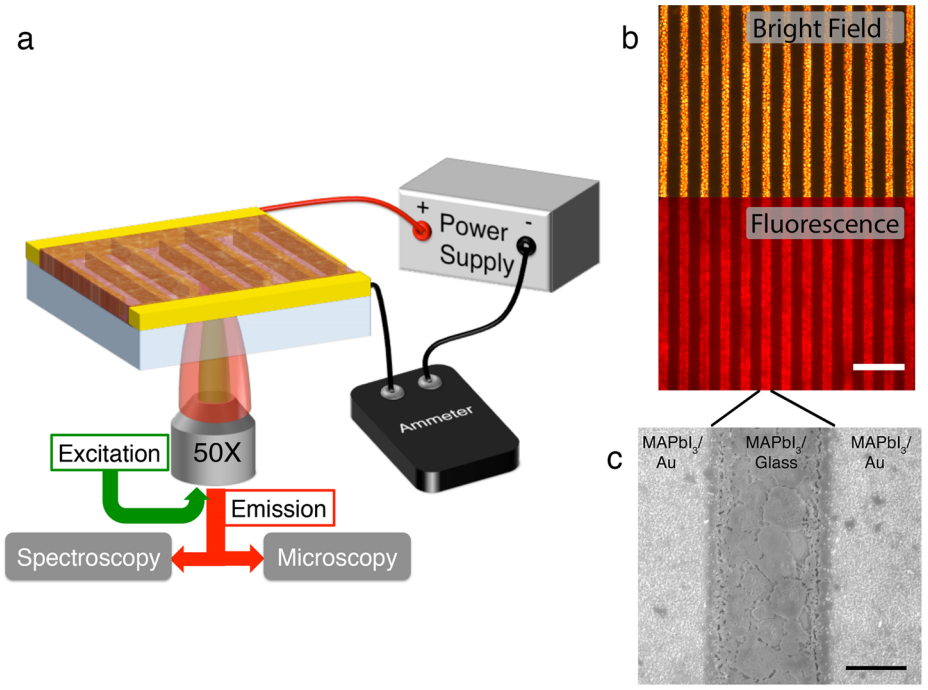

Figure 1. (a) Schematic of the testing platform used for the PL and current response to an applied electrical bias. (b) Optical microscope images of the full collected area in bright field mode (top) and fluorescence mode (bottom). The scale bar is 50 μm. (c) SEM image of the IDE device with $MAPbI_3$ showing good gap filling between the electrodes. Scale bar is 5 μm.

the PL response under bias,[13,50,51] but still at steady-state conditions. Based on the intrinsic sensitivity of the PL response to the material's electronic, compositional, and structural state, time-resolved PL on the time scale of the electrical slow transients will be a valuable technique to gain insight into the mechanisms behind the slow transient effects. In this work, we use a lateral interdigitated electrode (IDE) device coupled with time-resolved PL spectroscopy and microscopy as a platform to investigate the slow transient response to a step change in applied bias. We observed electric field-dependent slow transient optical responses in the forms of spatially and spectrally resolved PL quenching coupled with slow current transients. Analysis of these PL transient responses was capable of distinguishing between two simultaneous and independent phenomena; one was reversible, and the other was irreversible within the experimental time scales. Direct correlation of the optical and electrical transient responses indicates that the observed reversible response is a result of charge trapping whereas the irreversible response arises from defect ion migration under nominal electric fields.

2. EXPERIMENTAL METHODS

2.1. Material Synthesis. Methylammonium iodide (MAI) was synthesized by reacting methylamine (40 wt % in water) with equimolar amounts of HI (57 wt % in water) in ambient atmosphere at 0 °C for 2 h. The solution was dried in a rotoevaporator at 75 °C. The precipitate was washed three times with diethyl ether and dried at 50 °C in a vacuum oven. PbI_2 (99.9985% metals basis) was obtained from Alfa Aesar and used as received. The $MAPbI_3$ precursor solution was made by dissolving PbI_2 and MAI in DMF at 60 °C overnight.

2.2. Device Fabrication. The interdigitated gold electrodes on borofloat glass were provided by Vaporsens. The electrodes were cleaned by 30 s of sonication in acetone, methanol, and isopropyl alcohol separately followed by UV-ozone cleaning for 15 min. Clean electrodes were transferred to the spin coater under ambient conditions. The IDE surface was soaked with a drop of the $MAPbI_3$ precursor solution for 30 s before spinning at 4000 rpm for 15 s. The devices were immediately transferred to a hot plate and annealed at 120 °C for 30 min. The completed devices were then stored in a vacuum desiccator in the dark for at least 12 h before testing.

2.3. Device Characterization. X-ray diffraction (XRD) was preformed on the $MAPbI_3$ coated IDE in ambient atmosphere using a Panalytical X'Pert X-ray diffractometer. Current−voltage sweeps were performed under a low flow of argon with a Keithley 236 SMU. The scan rates for both dark and light measurements were 5 $V\,s^{-1}$.

2.4. Dynamic Photoluminescence Spectroscopy. The devices were transferred to a custom-designed chamber and placed on a Leica DMI4000 Fluorescence microscope. The chamber was purged with a low flow of argon for 15 min in the dark followed by a 15 min light soak. A mercury lamp supplied the excitation light through a long-pass optical filter to deliver 0.9 mW/cm^2 of 560 nm peak light through the bottom objective. The emitted light from the device was directed to either a high-resolution CCD camera for imaging or a Princeton Instruments Acton PIXIS:400B spectrophotometer for spectroscopy. Voltage was applied by an external power supply by pulsing between short circuit (0 V) and the desired bias level. In the negative bias, the leads connecting to the device were switched. Current was measured three times per second by monitoring the voltage change across a 10 kΩ resistor using a SigZig data logger from Vaporsens.

For the spectroscopy studies, a single device was used for all experiments unless otherwise noted. Between each experiment, the analysis spot was moved to a new region followed by light soaking for 15 min before measurement. Thus, while the entire IDE experienced every applied voltage, the light excitation was limited to a different area for each experiment to maintain a

DOI: 10.1021/acs.jpcc.5b11973
J. Phys. Chem. C 2016, 120, 7893−7902

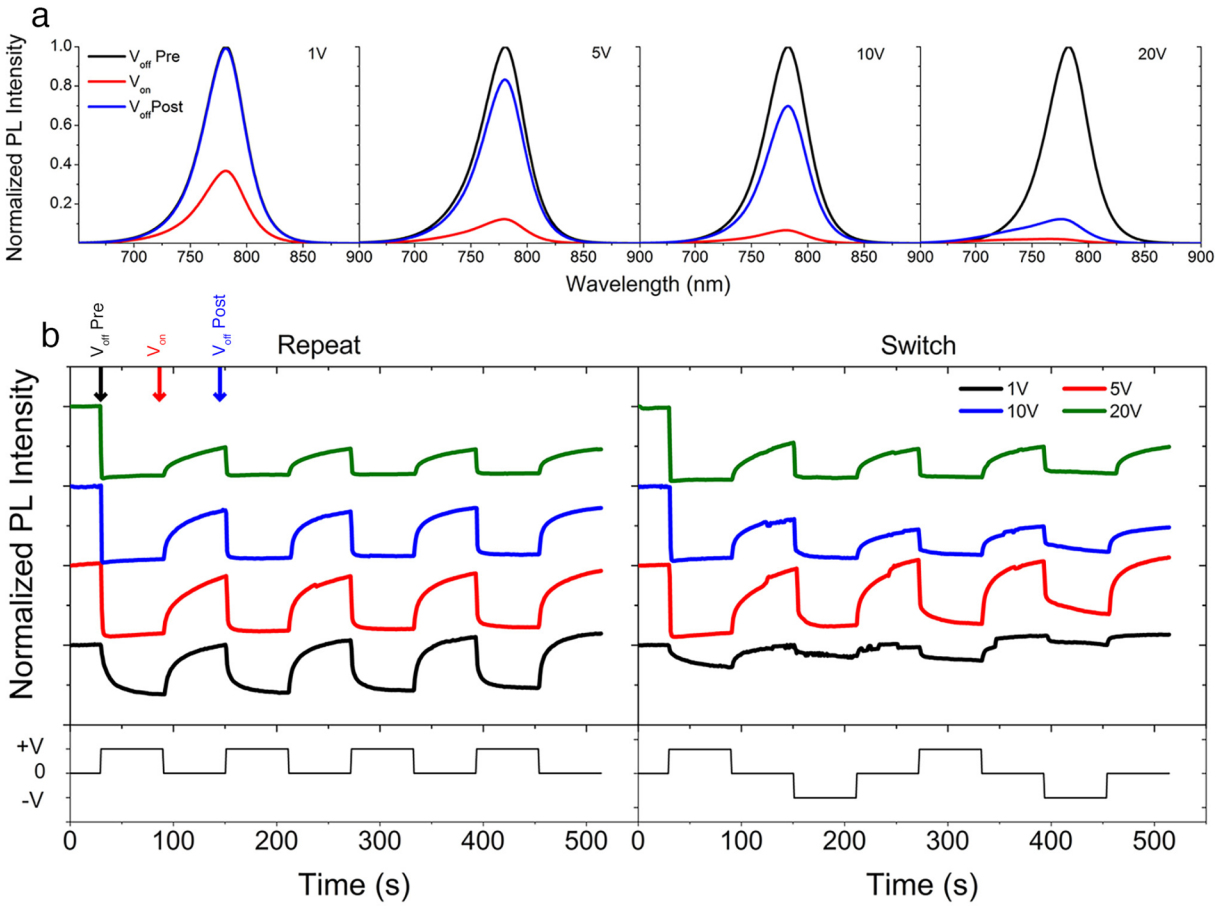

Figure 2. (a) Individual PL spectra taken from the time-resolved PL repeat experiment before, during, and after (black, red, and blue lines, respectively) the application of a 1, 5, 10, and 20 V bias. The isolated spectra frames correspond to the times represented by the matching color arrows seen in the time profiles in Figure 1b. The spectra at each voltage are normalized to the peak maximum of the prebias curve (black). (b) Time-resolved profile of the PL response to the applied bias for both repeat (left) and switch (right) experiments. The intensity represents the maximum peak value, which is normalized to the initial value and offset vertically to aid comparisons. The graphs below the PL response profiles represent the applied electrode polarity, where +V is the direction of the first applied voltage and the −V represents the polarity when the leads to the test structure were switched.

common initial state across all measurements. The order of experiments was repeated followed by switch at the same voltage magnitude. The applied biases started with 1 V and increased to 20 V for each experiment. The PL was measured for 30 s to establish a baseline PL before any voltage was applied. The PL intensity from each recorded spectrum was calculated by finding the peak maximum; therefore, any peak shifting was accounted for. Full spectra were recorded every 0.5 s, and the PL intensity was calculated from the peak maximum at each spectrum.

A separate device, fabricated following identical procedures, was used for dynamic PL imaging results. The exposure time for each frame was 6 s. A minimum of four frames were recorded to show the PL stability prior to bias application; the response under bias was measured for 10 frames, and 4−5 frames were used to show the recovery after bias removal. A new area was chosen for each voltage magnitude, but the positive and negative measurements at a particular voltage magnitude used the same area. Each new area underwent a 15 min light soak prior to testing. The time between the positive and negative voltage experiments was between 1 and 2 min.

3. RESULTS AND DISCUSSION

The multifunctional testing platform used for this study is shown schematically in Figure 1a. The test structure consisted of a symmetric gold IDE device with 10 μm wide electrodes and 10 μm electrode gap distances on a glass substrate. $MAPbI_3$ was deposited in a one-step spin coating technique directly onto the IDE test structure with no buffer layers. The $MAPbI_3$ showed fairly uniform coverage between the gold electrodes, as seen in the optical and SEM images in panels b and c of Figure 1, respectively. An XRD spectrum of a $MAPbI_3$ coated IDE device is seen in Figure S1 in the Supporting Information. The $MAPbI_3$ exhibited good Ohmic contact with the gold electrodes based on the linear and symmetric $I-V$ curves, as seen in Figure S2. The PL responses were measured with an inverted fluorescence microscope equipped with a high-resolution camera and a spectrophotometer. The electrical bias was applied using a power supply with an inline ammeter for simultaneous current monitoring. The applied biases used in this study were 1, 5, 10, and 20 V, equating to nominal in-plane electric fields ranging from 1 to 20 kV cm^{-1}. Comparatively, planar vertically stacked solar cell devices with a typical maximum power point voltage of 0.75 V across a thickness of up to 500 nm would experience an electric field of 15 kV cm^{-1} or higher. Thus, the applied fields used in this study are relevant

DOI: 10.1021/acs.jpcc.5b11973
J. Phys. Chem. C 2016, 120, 7893−7902

to the planar vertically stacked devices. As depicted in Figure 1a, green light excitation and PL emission collection occurred through the upward-facing objective with a spot size of 5×10^{-3} cm^2. Therefore, excitation of and emission from the $MAPbI_3$ was limited to the material between the electrodes, isolating the bias-dependent response. The IDE device has a small electrode interface area minimizing contribution from electrode interface effects compared to planar vertically stacked devices. The prepatterned electrodes apply a more uniform and controllable electric field across the sample compared to vertically stacked devices, which vary with the $MAPbI_3$ thickness. The electrode symmetry of the IDE device enables reliable studies on the electrode polarity to investigate the reversibility of the responses. Furthermore, the measurements occur across multiple electrode pairs over a relatively large measurement area, which should average out microscale nonuniformities in the $MAPbI_3$ morphology for consistent spectroscopy measurements. Finally, the IDE provides a large and redundant sampling area to effectively monitor spatially dependent PL changes relative to the electrode polarity. Thus, this testing platform effectively isolates the intrinsic $MAPbI_3$ response. The intrinsic response, however, is still dependent on the environmental conditions during fabrication and testing. A discussion on the sensitivity of this testing platform on the environmental conditions is included in the Supporting Information.

Two types of experiments were performed at the four voltages (denoted by V) to fully investigate the reversibility of the responses: (1) *repeat* tests, in which the applied voltage was repeatedly cycled between 0 and $+V$ for four cycles, and (2) *switch* tests, in which the electrode polarity was switched in the sequence 0, $+V$, 0, $-V$ for two complete cycles yielding four decays and four recovery responses. The 0 V state indicates a short circuit condition. Figure 2a shows spatially averaged PL spectra measured before, during, and after the first application of all biases during the repeat tests. In the absence of bias, a stable PL emission with a sharp single peak centered at 775 nm was observed, which is in good agreement with what is reported in the literature. Upon the application of any bias, quenching of the PL relative to the bias magnitude was observed. When the bias was removed, the PL intensity recovered over time; however, the ultimate degree of recovery was inversely related to the bias magnitude. Additionally, a slight blue shift of the PL peak (and appearance of a secondary peak at higher energy) was observed after applying 20 V bias and only partially recovered when the bias was removed. The spectra plotted on a log scale accentuating these subtle PL changes are shown in Figure S3.

The time-resolved PL response was monitored by tracking the PL intensity maximum of each spectrum to account for any slight shifts in the peak wavelength. The normalized time-resolved PL response profiles are displayed in Figure 2b and yield several important qualitative observations. Starting with the 1 V experiments, in particular the repeat test, a slow response was observed as a monotonic decay to a steady-state value that was consistent across all cycles and fully recoverable to the initial prebias state. Thus, for a bias of 1 V, the slow transient is considered to be completely reversible. [Note that there is a difference in the relative quenching efficiency and noise level between the 1 V repeat and 1 V switch responses seen in this device and other similar experiments (see Figure S4). The source of this variation is unknown and the subject of continued investigation, but it is important to note that the general trend of complete PL recovery after removal of the bias is still observed.] However, for both repeat and switch experiments at voltage magnitudes greater than 1 V, the PL response was dependent on the cycle number. In the first cycle at these larger biases, the response showed an overshoot behavior with fast PL quench to a minimum followed by a slow rise to the steady-state value. When the bias was removed, the PL response only partially recovered within the experimental time scales and the magnitudes of the recoveries were inversely related to the applied voltage magnitude, as previously highlighted in Figure 2a. Therefore, the initial response is considered to be at least partially irreversible. Alternatively, the second and subsequent cycles at these larger biases exhibited behaviors similar to the 1 V experiments with monotonic slow decays to the steady state established during the first cycle, and they were fully recoverable referenced to the beginning of the second cycle. Thus, under larger applied fields, there is clearly a unique interplay between distinctive reversible and irreversible processes.

The decay and recovery transients were quantified by graphical fitting to extract time constants, which are summarized in Figure 3. For the first responses of biases

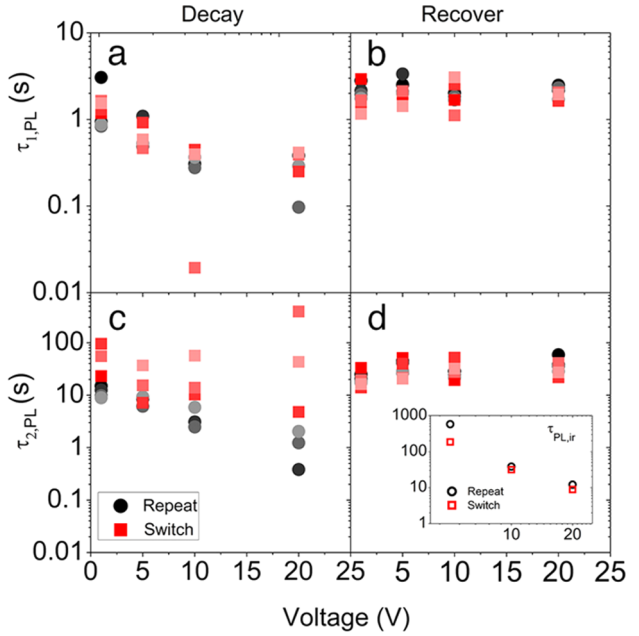

Figure 3. Summary of the fast $\tau_{1,PL}$ (a, b) and slow $\tau_{2,PL}$ (c, d) time constants from the isolated decay (a, c) and recover (b, d) response at each voltage. Both repeat (black circles) and switch (red squares) are shown. The response number is identified with decreasing color saturation of the red or black symbols. The gray dotted line represents the sensor exposure time. The inset in panel d summarizes the overshoot recovery response to an application of a bias greater than 1 V.

greater than 1 V, only the overshoot recovery (rise from the PL minimum to the steady-state value) was fit with a single-exponential function, and these time constants ($\tau_{PL,ir}$) are presented in the inset of Figure 3d. Alternatively, double-exponential functions were capable of fitting the complete monotonic decay and recover transients, revealing both fast ($\tau_{1,PL}$) and slow ($\tau_{2,PL}$) responses. Further discussion on the response fitting is supplied in the Supporting Information.

DOI: 10.1021/acs.jpcc.5b11973
J. Phys. Chem. C 2016, 120, 7893−7902

Figure 3 reveals a stark difference between the dynamics of decay and recovery and displays both commonalities and distinctions between the repeat and switch experiments. First, Figure 3a reveals a negative relation between the $\tau_{1,PL}$ and the applied voltage. The time constants range from 1 s to below 0.5 s. It is noted that the sensor exposure time used in these experiments was 0.5 s; therefore, the calculated time constants are ultimately limited to near 0.5 s and any value well below this limit is an artifact from the graphical fitting procedure. Thus, the $\tau_{1,PL}$ values for the 20 V experiments are likely limited by the instrument response time. The $\tau_{1,PL}$ values also show negligible deviations between cycle-to-cycle and between switch-and-repeat experiments at a particular voltage (including values above the instrument's response time), suggesting the mechanism is fully reversible upon removal of the bias. This reversibility is supported by the constant and consistent recovery transients across voltage and cycle number for both switch and repeat experiments. In contrast, the slower $\tau_{2,PL}$ decay constants differ significantly between the switch and repeat experiments. For the repeat tests, $\tau_{2,PL}$ also shows a negative correlation with the applied voltage and little cycle-to-cycle deviation, but $\tau_{2,PL}$ is an order of magnitude larger than $\tau_{1,PL}$ and well above the sensor exposure time. The negative correlation for $\tau_{2,PL}$ (repeat) was linear on a semilog scale, implying an exponential dependence, with a slope of -0.11 ± 0.02. Details concerning the fitting of the τ values with applied voltage are supplied in the Supporting Information. However, in the switch tests, the cycle-to-cycle scatter of $\tau_{2,PL}$ is large and increases both with bias magnitude and in a systematic manner with the cycle number. These trends may be more clearly visualized in the isolated and normalized response curves that were used for fitting, which are presented in Figure S5. The systematic increase of the response times after switching the electrode polarity suggests a repeated irreversible process. Despite the differences between the switch and repeat decay behaviors, the $\tau_{2,PL}$ recover transients for both switch and repeat again show a constant and consistent value across voltage and cycle number. This suggests a reversible process, similar to that seen in the repeat experiments, occurs simultaneously with and independently of the proposed irreversible process. To quantify this irreversible process, the $\tau_{PL,ir}$ trend is analyzed. As presented in the inset of Figure 3c, the $\tau_{PL,ir}$ values range from 10 to 100 s and also exhibit a negative correlation with the applied voltage. However, the slope on a semilog scale is best fit to -0.25, differentiating it from the reversible process.

In support of the PL transient responses, the simultaneously recorded dynamic current responses are presented in Figure 4.

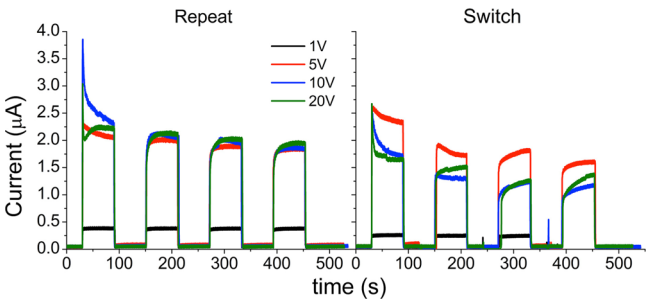

Figure 4. Time-resolved current response profile for repeat (left) and switch (right) experiments.

It is important to note that the PL and current transient responses show opposite sign (decrease/increase under bias respectively), and there was no clearly observable slow current transient decay when the bias was removed; therefore, only the transients in response to the application of a bias were analyzed. As seen in Figure 4, there are several qualitative similarities between the current and PL transients. First, the initial response to an applied bias greater than 1 V exhibited a peak and recovers to a steady-state value (with exception in the 20 V repeat response, which is discussed later). Subsequent responses in the repeat experiments, as well as all of the 1 V responses, showed only a monotonic rise to the steady-state value determined during the first response. Finally, the switch experiments showed systematic response variation upon switching the electrode polarity with biases above 1 V. The major qualitative difference between the current and PL transient responses is that the second switch response for 5 and 10 V biases also showed a peak and recover behavior similar to their first response. The subsequent responses in the switch experiments exhibited a monotonic increase, but not to any common steady-state value. The responses were fit using a similar procedure as the PL response fitting, namely, the monotonic transients were fit with a double-exponential function ($\tau_{1,I}$ and $\tau_{2,I}$), whereas the nonmonotonic responses only fit the recovery to steady state using a single exponential function ($\tau_{I,ir}$). Figure S6 presents the fitted time constants of the isolated current transients. The $\tau_{1,I}$ values appear to be mostly limited by the ammeter's sample rate (~0.25 s), but the $\tau_{2,I}$ values are well above that limitation with a similar magnitude to the $\tau_{2,PL}$ values (1−10 s for repeat and 10−100 s for switch experiments). However, unlike the PL responses, there was no clear voltage dependence in the $\tau_{2,I}$. The only voltage dependence that was observed was for $\tau_{I,ir}$, which shows a similar voltage dependence as the $\tau_{PL,ir}$ (see Figure S7). It is unclear why there was no voltage dependence for $\tau_{2,I}$; however, we note that, unlike the PL measurements, current was collected from the whole IDE device. Thus, dark current transients outside of the illuminated area (0.16 cm^2) may mask details of behavior within the illuminated region (5×10^{-3} cm^2) and make direct quantitative correlation between the current and PL responses beyond the scope of this paper.

Time-resolved PL imaging was used to further investigate the irreversibility and electrode polarity-dependent PL responses. The dynamic response was recorded with time-lapse PL images on a separate test structure to monitor the response to 1, 5, 10, and 20 V applied biases. In all experiments, the initial observation directly after application of an applied bias was a fast and uniform decrease in image brightness, which recovered when the bias was removed. However, when biases greater than 1 V were applied, some irreversible, localized PL quenching was observed. The time-lapse movies of +10 V and −10 V applied biases are presented in Supporting Information Movie 1 and Movie 2, respectively. Figure 5 shows an enlarged section of selected frames from these videos (full size images from Figure 5 are supplied in the Supporting Information). As seen in Movie 1, the first application of +10 V induced the formation of darker areas near the centers of the interelectrode gaps that grew from the centers toward the negative electrodes. Based on the SEM images in Figure 1c, the $MAPbI_3$ grain sizes are on the order of a micron and the observed quenched areas are half of the gap distance wide, 5 μm, and roughly 10 μm long; therefore, this quenched area encompasses several grains. Upon removal of the bias, the growth of the quenched areas stopped

DOI: 10.1021/acs.jpcc.5b11973
J. Phys. Chem. C 2016, 120, 7893−7902

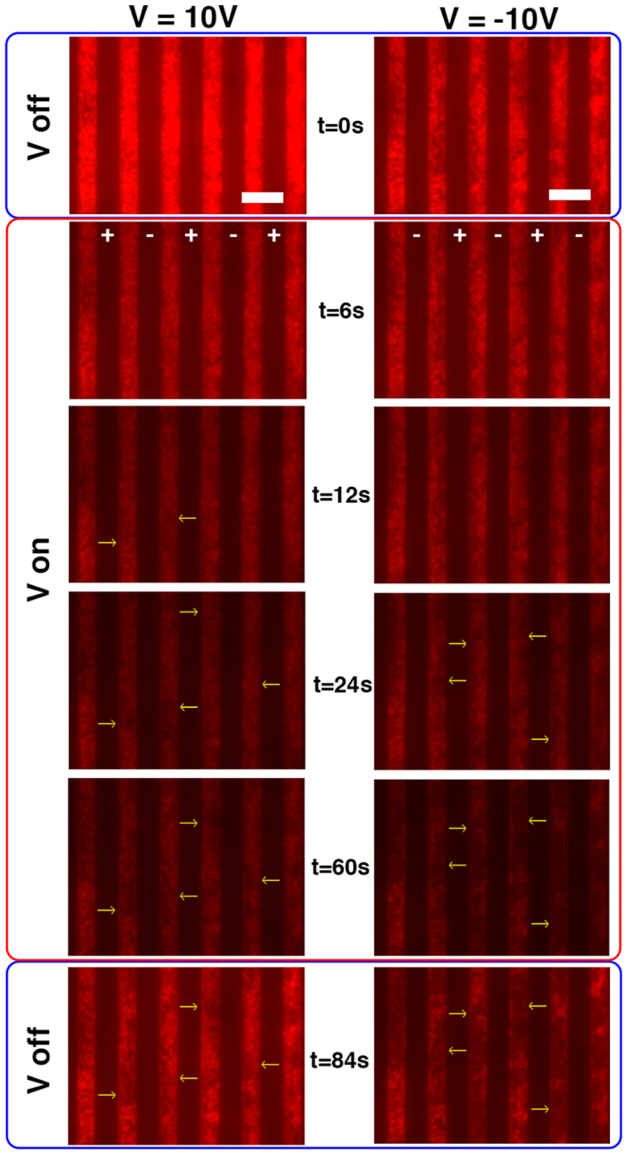

Figure 5. PL microscopy images showing the spatial-dependent PL response to +10 V (left panel) and −10 V biases (right panel). The images are cropped from frames taken from Movie 1 (+10 V) and Movie 2 (−10 V) in the Supporting Information. The listed time values represent the time from when the bias was applied, with 0 s being the frame directly before the application of the bias. Yellow arrows indicate the areas with the most notable changes in PL. The electrode polarity is labeled on the frame at t = 6 s when the bias is applied. The scale bars are both 20 μm.

but did not disappear with time, signifying a stable state under zero applied bias. As seen in Movie 2, reversing the electrode polarity (−10 V) on the same sample did not reverse the quenching in the areas formed during the +10 V test. Instead, new quenched areas nucleated at the now positive electrode and grew back toward the negative electrodes. Thus, the PL microscopy studies were capable of spatially resolving the reversible (uniform darkening of the PL images) and irreversible (stable quenched areas) PL responses correlating to the spectroscopy studies.

The results presented above highlight the complexity of the optoelectronic response of $MAPbI_3$ to an applied bias. The distinct reversible and irreversible responses signify that there are clearly multiple processes contributing to the slow transient responses. However, before these slow processes are analyzed, it is important to note the fast carrier dynamics that are expected to contribute to the magnitude of the PL and current response but cannot be resolved with the techniques used in this study. Under an applied bias, the free photogenerated charge carriers in the $MAPbI_3$ film will be swept out through the electrodes, resulting in fast PL quenching and a current spike, the rate of which is limited by the free carrier band-to-band recombination dynamics and drift velocities.[50,51] In $MAPbI_3$, the free carrier lifetimes have an upper bound on the order of hundreds of nanoseconds[46−48] and the mobilities have a lower bound[52] on the order of 1 $cm^2 V^{-1} s^{-1}$, leading to a transient time across the 10 μm gap of about 1 μs. This are clearly too fast to be resolved with the instrument response time (>0.5 s) and are therefore mixed with the $\tau_{1,PL/I}$ time constants. Thus, the full time-dependent current and PL responses are broken down into three regions, as depicted in Figure 6: (region I) steady state with no applied field, (region II) fast (nanosecond to microsecond time scales) free carrier response immediately after the field is applied, and (region III) slow (0.5−100 s time scales) transient response under constant applied field. Region III, as discussed above, is further identified as either an irreversible or reversible response. Based on the following analyses, these responses are attributed to ion migration and charge-trapping mechanisms, respectively.

The proposed relationship between ion migration and the resulting slow PL and current transients are depicted in Figure 6a. In a $MAPbI_3$ system, charged shallow defect ions, such as methylammonium and iodide interstitials (MA_i^+, $/I_i^-$) or vacancies (V_{MA}^-/V_I^+), are anticipated to have low formation energies[53,54] and low activation barriers for migration,[18,19] leading to potentially high concentrations of mobile ions. It is noted that details concerning defect formation, relative ratios of the various defect ions, and drift mobilities of the defect ions are still under debate and dependent on a number of experimental parameters beyond the scope of this paper. Under steady-state conditions prior to the application of the field (region I), the distributions of charged defects are expected to be uniform. When bias is applied (region II), charge carriers are swept out through the electrodes and produce a spike in the current and rapid PL quenching. Under continued application of a sufficient bias (V > 1 V) (region III), mobile ions respond by drifting toward their respective electrodes to partially compensate the external field. This field compensation reduces free carrier separation, leading to a slight increase in the PL and a decrease in the current. This response is similar to that seen in light-emitting electrochemical cells (LEECs), which use mobile molecular ions in a polymer matrix to dynamically adjust the electric field for enhanced charge injection at the electrode interface and radiative recombination in the bulk of the film. In fact, the first current response of the 20 V repeat experiment (double overshoot and recover to steady state) is similar to reported LEEC responses under sufficiently high fields where the buildup of charges decreases the injection barrier leading to an increase in the current.[55] When the external field is removed, the PL recovers, but not to the initial steady-state conditions, suggesting that any back diffusion of the mobile ions at room temperature is negligible.

The spatially resolved dynamic quenching from the PL images in Figure 5 and Movies 1 and 2 in the Supporting Information further support the irreversible ion migration mechanism as well as provide insight into the active mobile

DOI: 10.1021/acs.jpcc.5b11973
J. Phys. Chem. C 2016, 120, 7893−7902

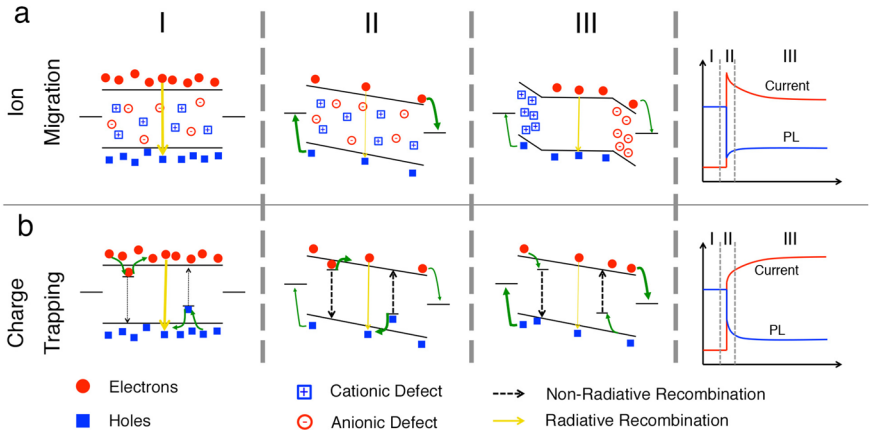

Figure 6. Schematic representation of the defect ion migration (top) and charge-trapping mechanisms (bottom) at equilibrium with the light excitation (I), immediately after the voltage is applied (II), and the slow transient response to the steady-state conditions (III). The far right column shows the expected current and PL responses correlating to regions I, II, and III.

species. When the voltage is first applied (+10 V), the quenching nucleates at the centers of the electrode gaps and moves toward the negative electrodes, supporting the hypothesis that the quenching is a result of drifting of a charged species. The areas with the most noticeable changes are highlighted with yellow arrows in Figure 5 and in the Supporting Information. The fact that the quenching nucleates at the center is important because if the quenching was caused by the build up or depletion of a defect ion, it should start at the electrode interface and grow inward following the concentration profile. Rather, these results suggest that the quenching mechanism is more complex and might involve multiple ions of opposite charge separating to form distinct compositional zones starting at the centers of the electrode gaps. In this case, because the quenched areas grow toward the negative electrodes, the quenching is initiated in areas with high MA^+/I^- ratios caused from drifting of either MA_i^+ and/or V_I^+ into the area. The stability of the quenched zones when the voltage is removed, and even when the electrode polarity is switched, signifies that the migration of the ions leads to a stable immobile state with decreased PL. Possible explanations for this immobile and stable quenched state include local stabilization of the shallow defect dopants leading to a decrease in the local radiative recombination lifetime, $\tau_{rad,p/n} = (R_{ec} \cdot N_{D/A})^{-1}$ (where R_{ec} is the recombination coefficient and $N_{D/A}$ is the donor/acceptor doping concentration), assuming a constant nonradiative recombination lifetime,[56] local compositional change leading to transformation of the shallow mobile defects to covalent immobile midgap recombination centers,[57] or compositional instability leading to degradation of the $MAPbI_3$ to PbI_2.[20] In fact, Leijtens et al. characterized the growth of PbI_2 in part through the observation of a PL peak near ~600 nm, which is attributed to highly defective PbI_2.[20] This is similar to the shoulder peak in Figure S3 that appears after the application of a 20 V bias, suggesting that a similar process may be contributing to the irreversible PL quenching. When the electrode polarity is reversed, new quenched areas nucleate at the now positive electrode and grow toward the negative electrode, signifying that despite the proposed defect ion stabilization process, excess mobile ions still remain in the material. The continual formation and growth of these stable PL quenched areas when the electrode polarity is reversed explains why the switch experiments show a systematic change in the PL and current transient responses. The stable quenched areas likely have different defect ion mobilities, so the ion migration is suppressed over time, explaining why not all switch responses show the peak−recover behavior expected following an ion migration as discussed above. Thus, there is strong evidence that the irreversible PL quenching behavior under sufficient applied bias is a result of ion migration, but the exact mechanism leading to the irreversible PL quenching still needs to be identified.

Based on the above analysis, the ion migration occurs only when the applied bias is above the threshold, 1 V, and when the electrode polarity is switched. Therefore, a charge-trapping mechanism is used to explain the 1 V experiments and the second through fourth transients of the repeat experiments as depicted in Figure 6b. Surface and interface traps in $MAPbI_3$ films are commonly cited as a potential source of the transient response,[11,58−60] but little is known about the atomistic or energetic details of these traps. In this system, the $MAPbI_3$ grains are on the order of 1 μm, compared to the 10 μm electrode gap distances, so there is significant surface and grain boundary interfacial area with potential trap states. Furthermore, no solvent annealing was performed on these samples; therefore, bulk crystal defects are also likely present. Prior to the application of the applied voltage (region I), the system is in steady state with the excess photogenerated charge carriers filling of the trap states to a steady-state level. When the bias is applied (region II), the excess photogenerated charge carriers are swept through the electrodes producing the current spike and sharp PL quenching before the traps can respond. The fast sweeping of both electron and holes reduces the photocarrier population, which in turn changes the trap dynamics. This leads to a slow emptying of the trap states, dependent on the trap energy and the emission rate from each trap, until a lower steady-state value is reached. This slow trap emission process (region III) provides a decaying source of excess free charge carriers leading to the slow monotonic increase and decrease in the current and PL, respectively. Furthermore, as the traps empty to the lower steady-state value under the applied bias, there will be an increase in the concentration of empty traps and therefore an increasing probability of a nonradiative recombination pathway for excess photogenerated carriers as the system reaches steady state. When the electrical bias is removed, the traps will fill as the concentration of the photogenerated carriers and trap states reach steady state. Within this context, the existence of the two transients ($\tau_{1,PL}$

DOI: 10.1021/acs.jpcc.5b11973
J. Phys. Chem. C 2016, 120, 7893−7902

and $\tau_{2,PL}$) could be explained by multiple traps with a range of energy levels and trap emission rates.

The above qualitative analysis correlates well with the trends seen in the isolated responses in Figure S5 but relies on the assumption that these mechanisms are independent from each other. However, because the mechanisms dynamically adjust the effective electric field and the free charge carrier population, for an ion migration and charge-trapping mechanism respectively, they are each ultimately affected by each other. Furthermore, the two processes occur simultaneously when the bias is applied, and each occurs over similar time scales. This makes detailed quantitative analysis of either mechanism extremely challenging and beyond the scope of this paper. Nevertheless, it is proposed that the IDE device used in this study was essential to differentiate these distinct processes. The 10 μm gap distances in the IDE device is much greater than the 500 nm thickness in the vertically stacked devices, which leads to longer ion transient times and larger spatial separation. This slowed the transient responses limited by the ion migration based on the increase in ion transient times across the larger distances and therefore created greater distinction between the reversible and irreversible responses. The ability to differentiate between each distinct mechanism is critical to gaining a deeper understanding of this material system. For example, in this system, a threshold for ion migration was found to be between 1 and 5 kV cm^{-1}, which is smaller than the electric fields used in optimized planar vertically stacked solar cell devices under working conditions (~15 kV cm^{-1}). While this threshold for migration is strongly dependent on material composition and morphology, which will vary widely across the different fabrication techniques and between the IDE and vertically stacked planar devices, it supports the growing evidence that ion migration likely contributes to the slow transient, and therefore hysteretic, behavior commonly reported in even the highest performing perovskite solar cell devices.

4. CONCLUSIONS

In summary, time-resolved photoluminescence was used to gain a deeper understanding of the source of the slow transient optoelectronic response in $MAPbI_3$. The kinetics of the slow PL transient responses revealed two distinct and independent processes, a reversible and an irreversible process. By correlating these results with the in situ time-resolved current response and PL imaging, the reversible and irreversible mechanisms were attributed to charge trapping and ion migration, respectively. The irreversible PL quenching was found to stem from ion migration creating compositionally distinct areas that remained stable under zero applied bias as well as reversed polarity. These findings are important because the threshold field for ion migration determined from this study (between 1 and 5 kV cm^{-1}) is smaller than the electric fields present in planar perovskite solar cells under working conditions (at or above 15 kV cm^{-1}). Thus, this work suggests that the slow transient effect leading to the observed hysteresis in optimized solar cell devices is the result of a complex response including both ion migration and charge trapping. We propose that the lateral IDE design was essential for identification of these distinct processes because it enhanced spatial separation and elongated the transient times to magnitudes that were easily detectable and distinguishable. Finally, we are confident that future systematic studies using this testing platform, coupled with additional structural and nanoscale characterization techniques, will be a vital contribution to unlocking the mysteries intrinsic to these remarkable hybrid organic perovskite materials.

■ ASSOCIATED CONTENT

Supporting Information

The Supporting Information is available free of charge on the ACS Publications website at DOI: 10.1021/acs.jpcc.5b11973.

$MAPbI_3$ coated IDE characterization, a note on the environmental sensitivity, graphical fitting details of the time-resolved current and PL responses, and details on the fitting of the voltage-dependent response kinetics (PDF)

Movie of the dynamic PL mapping in response to +10 V applied bias (MPG)

Movie of the dynamic PL mapping in response to −10 V applied bias (MPG)

Enlarged PL images from Figure 5 (PDF)

■ AUTHOR INFORMATION

Corresponding Author

*E-mail: lzang@eng.utah.edu.

Notes

The authors declare no competing financial interest.

■ ACKNOWLEDGMENTS

The authors thank Vaporsens for supplying the IDE test structures and the SigZig data logger and for their assistance with using the data logger for current measurements. This work was supported by the USTAR Program. B.R.B. was supported by the NASA Office of the Chief Technologist (NNX12AM67H). M.A.S. was supported by the U.S. Department of Energy, Office of Basic Energy Sciences, Division of Materials Sciences and Engineering (DE-SC0001630). B.R.B. and D.L.J. acknowledge support from the NSF IGERT (DGE0903715).

■ REFERENCES

(1) Jung, H. S.; Park, N.-G. Perovskite Solar Cells: From Materials to Devices. *Small* **2015**, *11*, 10−25.

(2) Park, N.-G. Organometal Perovskite Light Absorbers Toward a 20% Efficiency Low-Cost Solid-State Mesoscopic Solar Cell. *J. Phys. Chem. Lett.* **2013**, *4*, 2423−2429.

(3) Egger, D. A.; Edri, E.; Cahen, D.; Hodes, G. Perovskite Solar Cells: Do We Know What We Do Not Know? *J. Phys. Chem. Lett.* **2015**, *6*, 279−282.

(4) Snaith, H. J.; Abate, A.; Ball, J. M.; Eperon, G. E.; Leijtens, T.; Noel, N. K.; Stranks, S. D.; Wang, J. T.-W.; Wojciechowski, K.; Zhang, W. Anomalous Hysteresis in Perovskite Solar Cells. *J. Phys. Chem. Lett.* **2014**, *5*, 1511−1515.

(5) Kim, H.-S.; Park, N.-G. Parameters Affecting I−V Hysteresis of $CH_3NH_3PbI_3$ Perovskite Solar Cells: Effects of Perovskite Crystal Size and Mesoporous TiO2 Layer. *J. Phys. Chem. Lett.* **2014**, *5*, 2927−2934.

(6) Unger, E. L.; Hoke, E. T.; Bailie, C. D.; Nguyen, W. H.; Bowring, A. R.; Heumuller, T.; Christoforo, M. G.; McGehee, M. D. Hysteresis and Transient Behavior in Current-Voltage Measurements of Hybrid-Perovskite Absorber Solar Cells. *Energy Environ. Sci.* **2014**, *7*, 3690−3698.

(7) Gottesman, R.; Haltzi, E.; Gouda, L.; Tirosh, S.; Bouhadana, Y.; Zaban, A.; Mosconi, E.; De Angelis, F. Extremely Slow Photoconductivity Response of $CH_3NH_3PbI_3$ Perovskites Suggesting Structural Changes under Working Conditions. *J. Phys. Chem. Lett.* **2014**, *5*, 2662−2669.

(8) Tress, W.; Marinova, N.; Moehl, T.; Zakeeruddin, S. M.; Nazeeruddin, M. K.; Gratzel, M. Understanding the Rate-Dependent J-

DOI: 10.1021/acs.jpcc.5b11973
J. Phys. Chem. C 2016, 120, 7893−7902

V Hysteresis, Slow Time Component, and Aging in $CH_3NH_3PbI_3$ Perovskite Solar Cells: The Role of a Compensated Electric Field. *Energy Environ. Sci.* **2015**, *8*, 995−1004.
(9) Gonzalez-Pedro, V.; Juarez-Perez, E. J.; Arsyad, W.-S.; Barea, E. M.; Fabregat-Santiago, F.; Mora-Sero, I.; Bisquert, J. General Working Principles of CH3NH3PbX3 Perovskite Solar Cells. *Nano Lett.* **2014**, *14*, 888−893.
(10) Sanchez, R. S.; Gonzalez-Pedro, V.; Lee, J.-W.; Park, N.-G.; Kang, Y. S.; Mora-Sero, I.; Bisquert, J. Slow Dynamic Processes in Lead Halide Perovskite Solar Cells. Characteristic Times and Hysteresis. *J. Phys. Chem. Lett.* **2014**, *5*, 2357−2363.
(11) Shao, Y.; Xiao, Z.; Bi, C.; Yuan, Y.; Huang, J. Origin and Elimination of Photocurrent Hysteresis by Fullerene Passivation in $CH_3NH_3PbI_3$ Planar Heterojunction Solar Cells. *Nat. Commun.* **2014**, *5*, 5784.
(12) Juarez-Perez, E. J.; Sanchez, R. S.; Badia, L.; Garcia-Belmonte, G.; Kang, Y. S.; Mora-Sero, I.; Bisquert, J. Photoinduced Giant Dielectric Constant in Lead Halide Perovskite Solar Cells. *J. Phys. Chem. Lett.* **2014**, *5*, 2390−2394.
(13) Xiao, Z.; Yuan, Y.; Shao, Y.; Wang, Q.; Dong, Q.; Bi, C.; Sharma, P.; Gruverman, A.; Huang, J. Giant Switchable Photovoltaic Effect in Organometal Trihalide Perovskite Devices. *Nat. Mater.* **2014**, *14*, 193−198.
(14) Yuan, Y.; Chae, J.; Shao, Y.; Wang, Q.; Xiao, Z.; Centrone, A.; Huang, J. Photovoltaic Switching Mechanism in Lateral Structure Hybrid Perovskite Solar Cells. *Adv. Energy Mater.* **2015**, *5*, DOI: 10.1002/aenm.201500615.
(15) Deng, Y.; Xiao, Z.; Huang, J. Light-Induced Self-Poling Effect on Organometal Trihalide Perovskite Solar Cells for Increased Device Efficiency and Stability. *Adv. Energy Mater.* **2015**, *5*, DOI: 10.1002/aenm.201500721.
(16) Tress, W.; Marinova, N.; Moehl, T.; Zakeeruddin, S. M.; Nazeeruddin, M. K.; Gratzel, M. Understanding the Rate-Dependent J-V Hysteresis, Slow Time Component, and Aging in $CH_3NH_3PbI_3$ Perovskite Solar Cells: The Role of a Compensated Electric Field. *Energy Environ. Sci.* **2015**, *8*, 995−1004.
(17) Zhao, Y.; Liang, C.; Zhang, H.; Li, D.; Tian, D.; Li, G.; Jing, X.; Zhang, W.; Xiao, W.; Liu, Q.; et al. Anomalously Large Interface Charge in Polarity-Switchable Photovoltaic Devices: An Indication of Mobile Ions in Organic-Inorganic Halide Perovskites. *Energy Environ. Sci.* **2015**, *8*, 1256−1260.
(18) Eames, C.; Frost, J. M.; Barnes, P. R. F.; O'Regan, B. C.; Walsh, A.; Islam, M. S. Ionic Transport in Hybrid Lead Iodide Perovskite Solar Cells. *Nat. Commun.* **2015**, *6*, 7497.
(19) Azpiroz, J. M.; Mosconi, E.; Bisquert, J.; De Angelis, F. Defects Migration in Methylammonium Lead Iodide and Their Role in Perovskite Solar Cells Operation. *Energy Environ. Sci.* **2015**, *8*, 2118−2127.
(20) Leijtens, T.; Hoke, E. T.; Grancini, G.; Slotcavage, D. J.; Eperon, G. E.; Ball, J. M.; De Bastiani, M.; Bowring, A. R.; Martino, N.; Wojciechowski, K.; et al. Mapping Electric Field−Induced Switchable Poling and Structural Degradation in Hybrid Lead Halide Perovskite Thin Films. *Adv. Energy Mater.* **2015**, *5*, DOI: 10.1002/aenm.201500962.
(21) Frost, J. M.; Butler, K. T.; Brivio, F.; Hendon, C. H.; van Schilfgaarde, M.; Walsh, A. Atomistic Origins of High-Performance in Hybrid Halide Perovskite Solar Cells. *Nano Lett.* **2014**, *14*, 2584−2590.
(22) Bertoluzzi, L.; Sanchez, R. S.; Liu, L.; Lee, J.-W.; Mas-Marza, E.; Han, H.; Park, N.-G.; Mora-Sero, I.; Bisquert, J. Cooperative Kinetics of Depolarization in $CH_3NH_3PbI_3$ Perovskite Solar Cells. *Energy Environ. Sci.* **2015**, *8*, 910−915.
(23) Kutes, Y.; Ye, L.; Zhou, Y.; Pang, S.; Huey, B. D.; Padture, N. P. Direct Observation of Ferroelectric Domains in Solution-Processed $CH_3NH_3PbI_3$ Perovskite Thin Films. *J. Phys. Chem. Lett.* **2014**, *5*, 3335−3339.
(24) Wu, X.; Yu, H.; Li, L.; Wang, F.; Xu, H.; Zhao, N. Composition-Dependent Light-Induced Dipole Moment Change in Organometal Halide Perovskites. *J. Phys. Chem. C* **2015**, *119*, 1253−1259.
(25) Fan, Z.; Xiao, J.; Sun, K.; Chen, L.; Hu, Y.; Ouyang, J.; Ong, K. P.; Zeng, K.; Wang, J. Ferroelectricity of $CH_3NH_3PbI_3$ Perovskite. *J. Phys. Chem. Lett.* **2015**, *6*, 1155−1161.
(26) Grancini, G.; Srimath Kandada, A. R.; Frost, J. M.; Barker, A. J.; De Bastiani, M.; Gandini, M.; Marras, S.; Lanzani, G.; Walsh, A.; Petrozza, A. Role of Microstructure in the Electron−hole Interaction of Hybrid Lead Halide Perovskites. *Nat. Photonics* **2015**, *9*, 695−701.
(27) Leguy, A. M. A.; Frost, J. M.; McMahon, A. P.; Sakai, V. G.; Kochelmann, W.; Law, C.; Li, X.; Foglia, F.; Walsh, A.; O'Regan, B. C.; et al. The Dynamics of Methylammonium Ions in Hybrid Organic-Inorganic Perovskite Solar Cells. *Nat. Commun.* **2015**, *6*, DOI: 10.1038/ncomms8124.
(28) Zhu, F.; Men, L.; Guo, Y.; Zhu, Q.; Bhattacharjee, U.; Goodwin, P. M.; Petrich, J. W.; Smith, E. A.; Vela, J. Shape Evolution and Single Particle Luminescence of Organometal Halide Perovskite Nanocrystals. *ACS Nano* **2015**, *9*, 2948−2959.
(29) Nie, W.; Tsai, H.; Asadpour, R.; Blancon, J.-C.; Neukirch, A. J.; Gupta, G.; Crochet, J. J.; Chhowalla, M.; Tretiak, S.; Alam, M. A.; et al. High-Efficiency Solution-Processed Perovskite Solar Cells with Millimeter-Scale Grains. *Science* **2015**, *347*, 522−525.
(30) Eperon, G. E.; Burlakov, V. M.; Docampo, P.; Goriely, A.; Snaith, H. J. Morphological Control for High Performance, Solution-Processed Planar Heterojunction Perovskite Solar Cells. *Adv. Funct. Mater.* **2014**, *24*, 151−157.
(31) Im, J.-H.; Kim, H.-S.; Park, N.-G. Morphology-Photovoltaic Property Correlation in Perovskite Solar Cells: One-Step versus Two-Step Deposition of $CH_3NH_3PbI_3$. *APL Mater.* **2014**, *2*, 081510.
(32) Gao, H.; Bao, C.; Li, F.; Yu, T.; Yang, J.; Zhu, W.; Zhou, X.; Fu, G.; Zou, Z. Nucleation and Crystal Growth of Organic−Inorganic Lead Halide Perovskites under Different Relative Humidity. *ACS Appl. Mater. Interfaces* **2015**, *7*, 9110−9117.
(33) You, J.; Yang, Y.; Hong, Z.; Song, T.-B.; Meng, L.; Liu, Y.; Jiang, C.; Zhou, H.; Chang, W.-H.; Li, G.; et al. Moisture Assisted Perovskite Film Growth for High Performance Solar Cells. *Appl. Phys. Lett.* **2014**, *105*, DOI: 18390210.1063/1.4901510.
(34) Bi, C.; Wang, Q.; Shao, Y.; Yuan, Y.; Xiao, Z.; Huang, J. Non-Wetting Surface-Driven High-Aspect-Ratio Crystalline Grain Growth for Efficient Hybrid Perovskite Solar Cells. *Nat. Commun.* **2015**, *6*, 7747.
(35) Fu, F.; Kranz, L.; Yoon, S.; Löckinger, J.; Jäger, T.; Perrenoud, J.; Feurer, T.; Gretener, C.; Bücheler, S.; Tiwari, A. N. Controlled Growth of PbI2 Nanoplates for Rapid Preparation of $CH_3NH_3PbI_3$ in Planar Perovskite Solar Cells. *Phys. Status Solidi A* **2015**, *212*, 2708−2717.
(36) Galisteo-López, J. F.; Anaya, M.; Calvo, M. E.; Míguez, H. Environmental Effects on the Photophysics of Organic−Inorganic Halide Perovskites. *J. Phys. Chem. Lett.* **2015**, *6*, 2200−2205.
(37) Christians, J. A.; Miranda Herrera, P. A.; Kamat, P. V. Transformation of the Excited State and Photovoltaic Efficiency of $CH_3NH_3PbI_3$ Perovskite upon Controlled Exposure to Humidified Air. *J. Am. Chem. Soc.* **2015**, *137*, 1530−1538.
(38) Tian, Y.; Peter, M.; Unger, E.; Abdellah, M.; Zheng, K.; Pullerits, T.; Yartsev, A.; Sundstrom, V.; Scheblykin, I. G. Mechanistic Insights into Perovskite Photoluminescence Enhancement: Light Curing with Oxygen Can Boost Yield Thousandfold. *Phys. Chem. Chem. Phys.* **2015**, *17*, 24978−24987.
(39) Tian, Y.; Merdasa, A.; Unger, E.; Abdellah, M.; Zheng, K.; McKibbin, S.; Mikkelsen, A.; Pullerits, T.; Yartsev, A.; Sundström, V.; et al. Enhanced Organo-Metal Halide Perovskite Photoluminescence from Nanosized Defect-Free Crystallites and Emitting Sites. *J. Phys. Chem. Lett.* **2015**, *6*, 4171−4177.
(40) Eperon, G. E.; Stranks, S. D.; Menelaou, C.; Johnston, M. B.; Herz, L. M.; Snaith, H. J. Formamidinium Lead Trihalide: A Broadly Tunable Perovskite for Efficient Planar Heterojunction Solar Cells. *Energy Environ. Sci.* **2014**, *7*, 982−988.
(41) Pellet, N.; Gao, P.; Gregori, G.; Yang, T.-Y.; Nazeeruddin, M. K.; Maier, J.; Grätzel, M. Mixed-Organic-Cation Perovskite Photovoltaics for Enhanced Solar-Light Harvesting. *Angew. Chem., Int. Ed.* **2014**, *53*, 3151−3157.

DOI: 10.1021/acs.jpcc.5b11973
J. Phys. Chem. C 2016, 120, 7893−7902

(42) Kong, W.; Ye, Z.; Qi, Z.; Zhang, B.; Wang, M.; Rahimi-Iman, A.; Wu, H. Characterization of an Abnormal Photoluminescence Behavior upon Crystal-Phase Transition of Perovskite $CH_3NH_3PbI_3$. *Phys. Chem. Chem. Phys.* **2015**, *17*, 16405−16411.
(43) Docampo, P.; Ball, J. M.; Darwich, M.; Eperon, G. E.; Snaith, H. J. Efficient Organometal Trihalide Perovskite Planar-Heterojunction Solar Cells on Flexible Polymer Substrates. *Nat. Commun.* **2013**, *4*, DOI: 10.1038/ncomms3761.
(44) Abrusci, A.; Stranks, S. D.; Docampo, P.; Yip, H.-L.; Jen, A. K.-Y.; Snaith, H. J. High-Performance Perovskite-Polymer Hybrid Solar Cells via Electronic Coupling with Fullerene Monolayers. *Nano Lett.* **2013**, *13*, 3124−3128.
(45) Roiati, V.; Colella, S.; Lerario, G.; De Marco, L.; Rizzo, A.; Listorti, A.; Gigli, G. Investigating Charge Dynamics in Halide Perovskite-Sensitized Mesostructured Solar Cells. *Energy Environ. Sci.* **2014**, *7*, 1889−1894.
(46) Xing, G.; Mathews, N.; Sun, S.; Lim, S. S.; Lam, Y. M.; Gratzel, M.; Mhaisalkar, S.; Sum, T. C. Long-Range Balanced Electron- and Hole-Transport Lengths in Organic-Inorganic $CH_3NH_3PbI_3$. *Science* **2013**, *342*, 344−347.
(47) Stranks, S. D.; Eperon, G. E.; Grancini, G.; Menelaou, C.; Alcocer, M. J.; Leijtens, T.; Herz, L. M.; Petrozza, A.; Snaith, H. J. Electron-Hole Diffusion Lengths Exceeding 1 Micrometer in an Organometal Trihalide Perovskite Absorber. *Science* **2013**, *342*, 341−344.
(48) Shi, D.; Adinolfi, V.; Comin, R.; Yuan, M.; Alarousu, E.; Buin, A.; Chen, Y.; Hoogland, S.; Rothenberger, A.; Katsiev, K.; et al. Low Trap-State Density and Long Carrier Diffusion in Organolead Trihalide Perovskite Single Crystals. *Science* **2015**, *347*, 519−522.
(49) Stranks, S. D.; Burlakov, V. M.; Leijtens, T.; Ball, J. M.; Goriely, A.; Snaith, H. J. Recombination Kinetics in Organic-Inorganic Perovskites: Excitons, Free Charge, and Subgap States. *Phys. Rev. Appl.* **2014**, *2*, DOI: 10.1103/PhysRevApplied.2.034007.
(50) Tvingstedt, K.; Malinkiewicz, O.; Baumann, A.; Deibel, C.; Snaith, H. J.; Dyakonov, V.; Bolink, H. J. Radiative Efficiency of Lead Iodide Based Perovskite Solar Cells. *Sci. Rep.* **2014**, *4*, 6071.
(51) Hsiao, Y.-C.; Wu, T.; Li, M.; Hu, B. Magneto-Optical Studies on Spin-Dependent Charge Recombination and Dissociation in Perovskite Solar Cells. *Adv. Mater.* **2015**, *27*, 2899−2906.
(52) Wehrenfennig, C.; Eperon, G. E.; Johnston, M. B.; Snaith, H. J.; Herz, L. M. High Charge Carrier Mobilities and Lifetimes in Organolead Trihalide Perovskites. *Adv. Mater.* **2014**, *26*, 1584−1589.
(53) Buin, A.; Pietsch, P.; Xu, J.; Voznyy, O.; Ip, A. H.; Comin, R.; Sargent, E. H. Materials Processing Routes to Trap-Free Halide Perovskites. *Nano Lett.* **2014**, *14*, 6281−6286.
(54) Yin, W.-J.; Shi, T.; Yan, Y. Unusual Defect Physics in $CH_3NH_3PbI_3$ Perovskite Solar Cell Absorber. *Appl. Phys. Lett.* **2014**, *104*, 063903.
(55) deMello, J. C.; Tessler, N.; Graham, S. C.; Friend, R. H. Ionic Space-Charge Effects in Polymer Light-Emitting Diodes. *Phys. Rev. B: Condens. Matter Mater. Phys.* **1998**, *57*, 12951−12963.
(56) Sze, S. M.; Ng, K. K. *Physics of Semiconductor Devices*, 3rd ed.; John Wiley & Sons, Inc.: Hoboken, NJ, 2007.
(57) Agiorgousis, M. L.; Sun, Y.-Y.; Zeng, H.; Zhang, S. Strong Covalency-Induced Recombination Centers in Perovskite Solar Cell Material $CH_3NH_3PbI_3$. *J. Am. Chem. Soc.* **2014**, *136*, 14570−14575.
(58) Xu, J.; Buin, A.; Ip, A. H.; Li, W.; Voznyy, O.; Comin, R.; Yuan, M.; Jeon, S.; Ning, Z.; McDowell, J. J. Perovskite-Fullerene Hybrid Materials Suppress Hysteresis in Planar Diodes. *Nat. Commun.* **2015**, *6*, 7081.
(59) Noel, N. K.; Abate, A.; Stranks, S. D.; Parrott, E. S.; Burlakov, V. M.; Goriely, A.; Snaith, H. J. Enhanced Photoluminescence and Solar Cell Performance via Lewis Base Passivation of Organic−Inorganic Lead Halide Perovskites. *ACS Nano* **2014**, *8*, 9815−9821.
(60) van Reenen, S.; Kemerink, M.; Snaith, H. J. Modeling Anomalous Hysteresis in Perovskite Solar Cells. *J. Phys. Chem. Lett.* **2015**, *6*, 3808−3814.

DOI: 10.1021/acs.jpcc.5b11973
J. Phys. Chem. C 2016, 120, 7893−7902